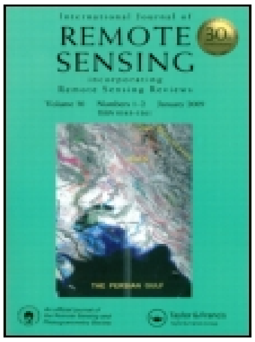

International Journal of Remote Sensing

ISSN: 0143-1161 (Print) 1366-5901 (Online) Journal homepage: http://www.tandfonline.com/loi/tres20

A dynamic scaling algorithm for the optimized digital display of VIIRS Day/Night Band imagery

Curtis J. Seaman & Steven D. Miller

To cite this article: Curtis J. Seaman & Steven D. Miller (2015) A dynamic scaling algorithm for the optimized digital display of VIIRS Day/Night Band imagery, International Journal of Remote Sensing, 36:7, 1839-1854, DOI: 10.1080/01431161.2015.1029100

To link to this article: https://doi.org/10.1080/01431161.2015.1029100

Published online: 01 Apr 2015.

Submit your article to this journal

Article views: 217

View Crossmark data

Citing articles: 2 View citing articles

Full Terms & Conditions of access and use can be found at
http://www.tandfonline.com/action/journalInformation?journalCode=tres20

International Journal of Remote Sensing, 2015
Vol. 36, No. 7, 1839–1854, http://dx.doi.org/10.1080/01431161.2015.1029100

Taylor & Francis
Taylor & Francis Group

A dynamic scaling algorithm for the optimized digital display of VIIRS Day/Night Band imagery

Curtis J. Seaman* and Steven D. Miller

Cooperative Institute for Research in the Atmosphere, Colorado State University, Fort Collins, CO 80523-1375, USA

(*Received 16 January 2015; accepted 7 March 2015*)

The VIIRS Day/Night Band (DNB) is a visible and near-infrared sensor that is sensitive to a broad range of light intensities ranging from daylight down to airglow at night. The on-board calibration of the DNB allows for the quantification of radiance values over the full range of the instrument's sensitivity, unlike the heritage Operational Linescan System (OLS). For scenes that span the day/night terminator, observed DNB radiance values may vary by up to eight orders of magnitude. Consequently, it is impractical to display the full range of radiance values in a single digital image. In this work, an algorithm is presented that scales the observed radiance values between expected maximum and minimum values that are a function of solar and lunar zenith angles as well as the fraction of the lunar disc that is illuminated by the Sun. This dynamic scaling algorithm preserves scene contrast over the full range of solar and lunar illumination conditions, similar to the Near Constant Contrast (NCC) imagery product. Unlike the NCC algorithm, however, the 'erf-dynamic scaling' algorithm (so-called for its likeness to the Gauss error function) presented here requires no ancillary information outside of what is included in the DNB data distributed according to the Joint Polar Satellite System (JPSS) program file standards. Results indicate that this algorithm has improved performance over simple methods for displaying DNB imagery and, in some instances, may exceed the performance of the NCC product itself. This algorithm is expected to replace many *ad hoc* methods of displaying DNB imagery and may serve as a substitute for operational users that do not have access to the NCC product.

1. Introduction

The Day/Night Band (DNB) is one of the 22 channels that comprise the Visible Infrared Imaging Radiometer Suite (VIIRS) (Lee et al. 2006; Hillger et al. 2013) carried on board the Suomi National Polar-orbiting Partnership (S-NPP) satellite. It is the second generation of what have been called 'low-light visible' sensors (Miller et al. 2013), based on the heritage Defense Meteorological Satellite Program (DMSP) Operational Linescan System (OLS). Similar to the OLS, the DNB is panchromatic (full width/half maximum response from 500 nm to 900 nm) and is sensitive over the range of intensities from full sunlight reflection (order 10^{-2} W cm^{-2} sr^{-1}) down to airglow at night (order 10^{-10} W cm^{-2} sr^{-1}). With a minimum detectable radiance of ~2×10^{-10} W cm^{-2} sr^{-1} at nadir (Liao et al. 2013), the DNB is sensitive enough to detect a single isolated street lamp from orbit (~834 km above the Earth) (Miller et al. 2013).

One of the many improvements of the DNB over the OLS is the on-board calibration of observed DNB radiance values (Liao et al. 2013; Liang et al. 2014). The OLS does not

---

*Corresponding author. Email: Curtis.Seaman@colostate.edu

© 2015 Taylor & Francis

record calibrated radiance data. Instead, relative brightness counts are recorded in 6-bit quantization using the OLS Gain Management Algorithm (GMA), which was designed to maintain a nearly constant scene contrast during the satellite's transition from daytime to twilight to night-time scenes and *vice versa*. The OLS GMA dynamically adjusts the gain based on solar elevation angle, lunar elevation angle, and relative azimuth angle using Gain Value Versus Scene Solar (and Lunar) Elevation (GVVSSE and GVVSLE) lookup tables (Liang et al. 2014). Whereas the OLS is sensitive to radiance values spanning seven to eight orders of magnitude, the GMA and 6-bit quantization effectively limit the dynamic range of the OLS to less than two orders of magnitude at any given time (Liang et al. 2014). In contrast, the DNB utilizes three gain stages and 13–14-bit quantization along with an on-board calibration (Liao et al. 2013; Mills et al. 2010; Geis et al. 2012) to provide unsaturated radiances over the full dynamic range of the sensor at all times during nominal operation. These calibrated radiances are recorded as floating point values in the VIIRS DNB Sensor Data Record (SDR) files.

As a result of the wide dynamic range of the DNB, the digital display of DNB imagery using the SDR data is not straightforward, particularly for scenes that transition from day to night or vice versa. Common image file formats (e.g. JPG, GIF, PNG, etc.) and display software (e.g. McIDAS {Man-computer Interactive Data Access System; http://www.ssec.wisc.edu/mcidas/}, AWIPS {Advanced Weather Interactive Processing System} (Seguin 2002), IDL {Interactive Data Language; http://www.exelisvis.com/ProductsServices/IDL.aspx}, matlab {http://www.mathworks.com/products/matlab/}, etc.) are limited to 256 colours for a single-channel image. Many operational forecast offices in the United States National Weather Service (NWS), the primary users of DNB imagery, utilize the N-AWIPS display software,[1] which is currently limited to 96 colours.

Expressing an eight-order-of-magnitude range of floating point values in 256 (or 96) colours without loss of information at the high or low ends of the dynamic range is not practical, even when utilizing a logarithmic scale. Figure 1 shows examples of DNB imagery that span the day/night terminator, rendered using simple linear and logarithmic

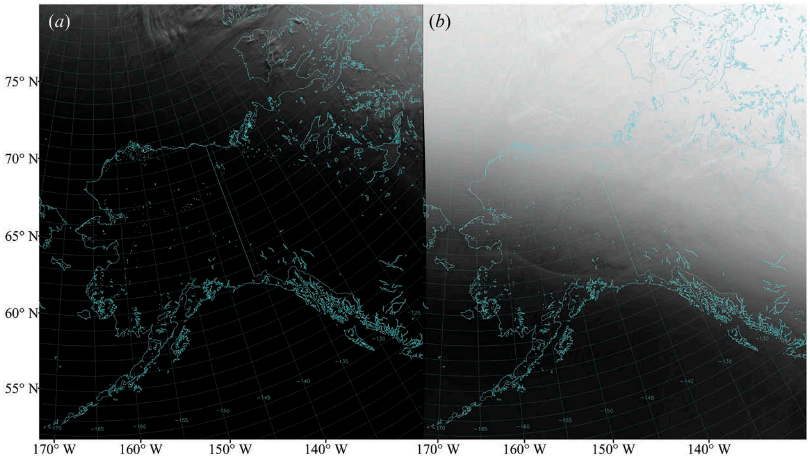

Figure 1. Examples of DNB imagery produced using (*a*) simple linear and (*b*) logarithmic scaling for a scene spanning the day/night terminator. Data for these images were collected at 11:56 UTC 1 May 2013.

scaling where the digital value of 0 (black) corresponds to the minimum radiance (or minimum base-10 logarithm of the radiance) in the scene and the digital value of 255 (white) corresponds to the maximum radiance (or maximum base-10 logarithm of the radiance) in the scene. In both examples, it is very difficult to identify clouds or surface features that would be of interest to operational forecasters over the majority of the scene.

To mitigate this problem, the Near Constant Contrast (NCC) algorithm (Liang et al. 2014) was developed and is implemented operationally as an Environmental Data Record (EDR) through the Joint Polar Satellite System (JPSS) program. The NCC algorithm converts the observed DNB radiance values into ‘pseudo-albedo’ values, reducing the dynamic range of the data from eight orders of magnitude to three orders of magnitude while maintaining nearly constant contrast across day, night, and twilight scenes. The original NCC algorithm was based on similar GVVSSE/GVVSLE tables and assumptions that were present in the OLS GMA that do not hold for the DNB (Liang et al. 2014). This limited the use of NCC imagery at night to scenes within 2–3 days of a full moon from first launch (28 October 2011) until a fix was implemented operationally on 10 July 2013.

Although the NCC algorithm has since been improved to work under all natural lighting conditions (i.e. day, night, and twilight) throughout the lunar cycle (Liang et al. 2014), the NCC EDR product has not gained widespread use within the operational user community. As a result of having to fix the initial errors in the NCC algorithm, the NCC EDR was the last VIIRS imagery product to reach the ‘Beta’ and ‘Provisional’ levels of maturity within the JPSS program (see http://www.jpss.noaa.gov/science-maturity-level.html and http://www.star.nesdis.noaa.gov/jpss/AlgorithmMaturity.php). This delayed the distribution of the NCC product to the operational users. Direct Broadcast sites for distribution of JPSS data products in near-real time have, in general, given primary attention to the production and distribution of SDR data products and have been slow to implement and distribute the NCC and other EDR imagery products. Furthermore, limitations on bandwidth have made numerous operational forecast offices reluctant to acquire NCC imagery in addition to the voluminous DNB SDR data they are already receiving. Instead, operational user groups have generally relied upon *ad hoc* methods for displaying the DNB SDR data.

For the above-stated reasons, it would be desirable for those with established DNB SDR data feeds to have a simple, dynamic, and readily portable automated algorithm for scaling the data to provide useful imagery under all natural lighting conditions throughout the lunar cycle. The objective is to approximate the NCC EDR product using only information contained in the DNB SDR files without the need for users to acquire additional data products or generate auxiliary data sets. In this work, we present such an algorithm. A key benefit of this algorithm is that there is no need to create, acquire, or maintain GVVSSE/GVVSLE tables or any other ancillary information. All of the necessary information is present within the DNB SDR data files and their associated geolocation files.

The article is outlined as follows. Section 2 provides an overview of the DNB SDR data and details the data used to validate the algorithm. Section 3 describes the dynamic scaling algorithm. Imagery produced using the scaling algorithm is presented and compared with the operational NCC imagery product in Section 4. Discussion and conclusions follow in Section 5.

2. Data

A full description of the VIIRS data files and products may be found in the Algorithm Theoretical Basis Documents (ATBD), Operational Algorithm Description (OAD) documents, and the Common Data Format Control Books (CDFCB) provided by the JPSS program. These documents are available online at http://npp.gsfc.nasa.gov/documents.html and http://www.star.nesdis.noaa.gov/jpss/ATBD.php. Next follows a brief summary of the salient information relevant to this work.

The production of geo-referenced VIIRS imagery requires both calibrated radiance (or reflectance or brightness temperature) data and the geolocation data, which are stored as separate files. For the DNB and NCC data, the geolocation files contain, for each pixel, latitude, longitude, solar azimuth and zenith angles, lunar azimuth and zenith angles as well as satellite viewing azimuth and zenith angles. The data are packaged as 'granules', with each granule containing ~86 s of collected data. With each granule, the fraction of the illuminated lunar disc that is observable from the Earth during that time period is reported. The DNB geolocation files also contain the lunar phase angle reported on a per-granule basis. Details of the on-orbit radiometric and geolocation accuracy of the S-NPP DNB are presented in Liao et al. (2013). All of the DNB radiance data used in this study were collected after stray-light correction (Mills, Weiss, and Liang 2013) was implemented operationally (10 July 2013), and the algorithm presented in the next section assumes the radiance values have been corrected for these artefacts.

The objective of this work is to develop a scaling algorithm for DNB data that provides useful imagery under all natural lighting conditions throughout the lunar cycle and for all regions of the globe. To develop this algorithm, DNB data from S-NPP were collected over two full orbits (i.e. containing both daytime and night-time scenes) on days with a full moon, new moon, last quarter moon, and three days after the first quarter moon. Table 1 presents the dates, times, and orbits from which data were collected for this study. Each orbit of data contains 70–72 granules, with each granule containing 4064 × 768 pixels for the DNB SDR, yielding more than 200 million data points per orbit.

S-NPP is in a Sun-synchronous orbit with an equator-crossing time of ~13:30 local time (LT) for the ascending node and ~01:30 LT for the descending node, with each orbit defined by successive ascending equator crossings. Recall that, to first order for an observer on the Earth, the moon reaches maximum zenith at local midnight for a full moon, local noon for a new moon, sunrise (~06:00 LT) for the last quarter, and sunset (~18:00 LT) for the first quarter. Therefore, the 01:30 LT descending overpass occurs ~90 min after the local moonset time on a night with a first quarter moon. The moon is not above the horizon for the night-time overpass until two to three nights after the first quarter. Similarly, the moon is above the horizon for S-NPP night-time orbits until two to three nights after the last quarter. Thus, data from the day of a first quarter moon would

Table 1. Dates, times, and S-NPP orbit numbers for the data-collection periods used in this study.

Case type	Orbit number	Start time (UTC)	End time (UTC)
First Quarter*	14367	2014/08/06 00:24	2014/08/06 02:06
	14374	2014/08/06 12:15	2014/08/06 13:56
Full Moon	14012	2014/07/12 00:01	2014/07/12 01:35
	14019	2014/07/12 11:43	2014/07/12 13:24
Last Quarter	14096	2014/07/17 21:59	2014/07/17 23:40
	14104	2014/07/18 11:31	2014/07/18 13:12
New Moon	14210	2014/07/25 22:49	2014/07/26 00:30
	14218	2014/07/26 12:21	2014/07/26 14:02

Note: *6 August 2014 was not the date of the first quarter moon, but was three days after the first quarter, as described in the text. Dates are provided in YYYY/MM/DD HH:SS format.

not be significantly different from data collected during a new moon. A complete study of lunar availability as a function of time, location, and for various orbits is presented in Miller, Combs, et al. (2012).

The orbits listed in Table 1 were selected according to the expected brightness of the background surface. For each case in Table 1, an orbit was chosen with the ascending node over Africa and Europe whereas the other orbit was chosen to have the ascending node over the Pacific Ocean. These orbits have descending nodes over the Pacific Ocean and over Africa, respectively. Thus, the observed radiance values over the Pacific Ocean (whose surface is poorly reflective at DNB wavelengths outside of Sun- and moon-glint) could be contrasted with the observed radiance values over the Sahara Desert (a highly reflective background at DNB wavelengths). In addition, Europe at night contains many city lights, which do not change as a function of lunar phase. It is expected that these two orbits capture the majority of the natural range in background surface brightness across the globe.

An additional test, not shown or further discussed, compared the observed radiance values for full-moon nights when the moon was near apogee and near perigee in its orbit. This was found not to have a significant impact on the observed radiance values or the resulting imagery created using the algorithm described in the next section. It has been estimated that the extremes of perigee-syzygy (referred to as 'supermoon') and apogee-syzygy (referred to as 'micromoon') differ by ~33% (Miller and Turner 2009).

3. Algorithm description

To first order, the primary cause of variability in the observed DNB radiance values is the presence or absence of sunlight. Figure 2 shows a scatter plot of the observed radiances as a function of solar zenith angle for the full-moon case identified in Table 1. This data has been divided into bins of 1° in solar zenith angle. For each bin, the mean, median, upper quartile, and lower quartile radiances were calculated. These values are included on Figure 2 as the thin grey curves overlaid on the region of scatter. Note the relatively consistent radiance values between ~1×10^{-2} and ~3×10^{-4} W cm^{-2} sr^{-1} for solar zenith angles <75° (daytime scenes), the more highly variable radiance values generally between 3×10^{-7} and 3×10^{-10} W cm^{-2} sr^{-1} for solar zenith angles >105° (night-time scenes), and the sharp transition from daytime radiances to night-time radiances for solar zenith angles between 75° and 105° (terminator scenes from near sunset to twilight). Some large outliers exist on the night-time side of the range. Occasional night-time radiance values above 3 x 10^{-7} W cm^{-2} sr^{-1} are likely due to city lights, lightning, and gas flares or other fires. Radiance values below 1×10^{-10} W cm^{-2} sr^{-1} are likely artefacts from the stray-light correction (Mills, Weiss, and Liang 2013) and the dark offsets used in the DNB calibration (Liao et al. 2013).

From these data we seek functions that dynamically capture the maximum and minimum expected radiances of atmospheric and background surface features relevant to operational forecasting objectives as a function of solar (and lunar) zenith angles. This would allow for optimal radiance scaling within this range and would produce a simple form of near-constant contrast imagery. An example of a typical scaling algorithm for infrared (IR) imagery would be of the following form:

$$B = 0 \leq 255\left(\frac{T_{\mathrm{b}} - T_{\mathrm{min}}}{T_{\mathrm{max}} - T_{\mathrm{min}}}\right) \leq 255, \qquad (1)$$

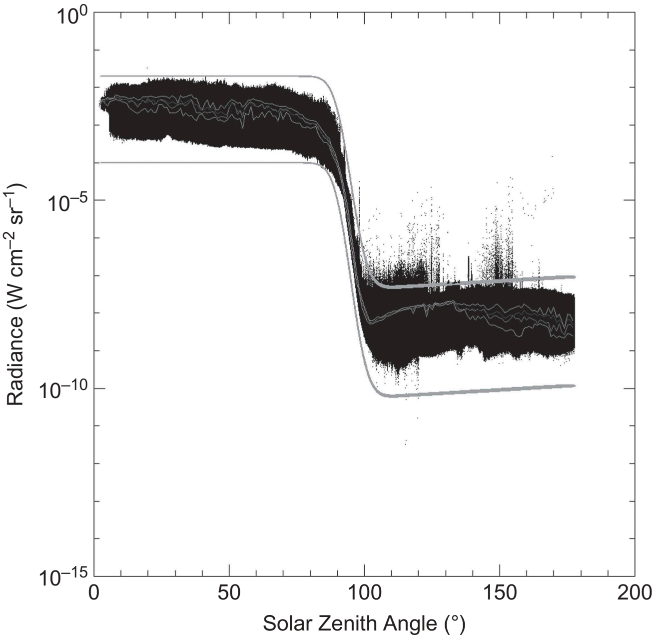

Figure 2. Scatter plot of the observed DNB radiance values as a function of solar zenith angle for the full-moon orbits in Table 1. Thin grey curves overlaid on the region of scatter are, from the lowest to the highest, lower quartile, median, mean, and upper quartile radiance for 1° solar zenith angle bins. The thick grey curves above and below the scatter represent the maximum and minimum radiance values, R_{max} and R_{min}, respectively, defined by the scaling algorithm described in the text. Note that the ordinate is plotted on a logarithmic scale.

where B is the resulting brightness index value (8-bit integer) for a given brightness temperature, T_{b}, that falls within the range of the preselected maximum and minimum brightness temperatures, T_{max} and T_{min}, respectively. Values of T_{b} greater than T_{max}, where the fraction in Equation (1) has a value above unity, are capped at a brightness index value of 255 and values of T_{b} less than T_{min} are set to zero. Similarly, for this work, we define the brightness index value, B, for a given radiance, R, as

$$B = 0 \leq 255\left(\frac{R - R_{\mathrm{min}}}{R_{\mathrm{max}} - R_{\mathrm{min}}}\right) \leq 255, \tag{2}$$

where R_{max} and R_{min} are the maximum and minimum radiance values, which, as discussed below, are defined dynamically as functions of the solar and lunar zenith angles and the fraction of the lunar disc that is illuminated.

The functional relationship adopted here is based on the so-called ‘error function’. For a variable, z, the error function is defined by

$$\mathrm{erf}(z) = \frac{2}{\sqrt{\pi}}\int_{0}^{z} e^{-t^{2}}\,\mathrm{d}t. \tag{3}$$

For a normal distribution characterized by the mean, μ, and standard deviation, σ, the cumulative distribution function is given by

$$D(z) = \frac{1}{2}\left[1 + \operatorname{erf}\left(\frac{z-\mu}{\sigma\sqrt{2}}\right)\right]. \tag{4}$$

Examples of the cumulative distribution functions for varying values of μ and σ are shown in Figure 3.

Here, we want to scale this cumulative distribution function to fit the upper and lower bounds of the observations shown in Figure 2. To do this, we define the scaling parameters, L_1 and L_2, the offset solar zenith angle, θ_0, and the slope parameter, s_0, such that the scaled cumulative distribution function, S, as a function of solar zenith angle, θ_{SZA}, is given by

$$S(\theta_{\text{SZA}}) = -L_1 - L_2\left[1 + \operatorname{erf}\left(\frac{\theta_{\text{SZA}} - \theta_0}{s_0\sqrt{2}}\right)\right]. \tag{5}$$

Hereafter, we will refer to S as the 'erf-dynamic scaling' (EDS) function. We define two such functions, $S_{\max}$ and $S_{\min}$, such that $R_{\max} = 10^{S_{\max}}$ and $R_{\min} = 10^{S_{\min}}$ define the maximum and minimum radiance values for the scaling function (Equation (2)). Note that it is not assumed that the observed radiance values are normally distributed. As may be inferred from Figure 2, a histogram of the observed radiance values would form a bimodal distribution, with one mode representing daytime radiances and the other mode representing night-time radiances. This algorithm simply uses the form of the cumulative distribution function, transformed into log-space by the definitions of $R_{\max}$ and $R_{\min}$, to approximate the range in the observed radiance values as a function of the solar zenith angle.

The first scaling parameter, L_1, controls the upper asymptote of the EDS function, which here represents the daytime radiance values. For $S_{\max}$ and $S_{\min}$, the values $L_{1_{\max}} =$

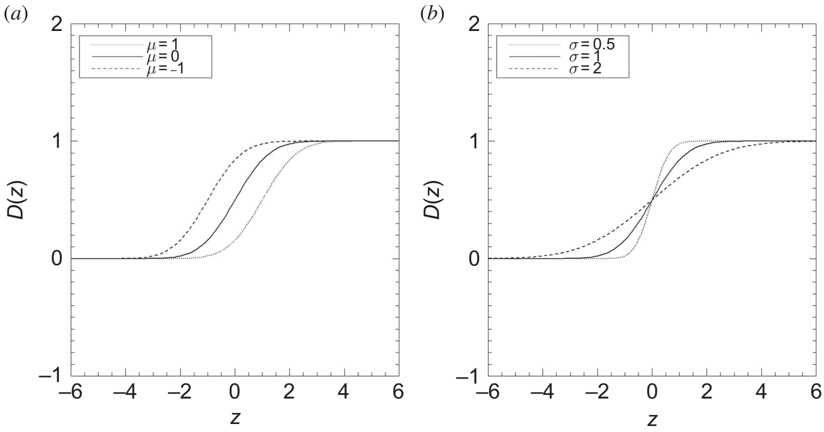

Figure 3. Examples of the cumulative distribution function (*a*) for the case of $\sigma = 1$ and μ varying between −1 and +1; and (*b*) for the case of $\mu = 0$ and σ varying between 0.5 and 2.

1.7 and $L_{1_{\text{min}}} = 4.0$ are used, which yield values of $R_{\text{max}} \approx 10^{-1.7} \approx 2 \times 10^{-2}$ W cm^{-2} sr^{-1} and $R_{\text{min}} \approx 1 \times 10^{-4}$ W cm^{-2} sr^{-1} for values of θ_{SZA} less than ~80°.

The offset solar zenith angle, θ_0, and slope parameter, s_0, control the centre solar zenith angle and slope, respectively, of the transition zone between daytime and night-time radiance values. As the solar zenith angle of 95° is approximately the centre of the transition zone from daylight to night-time, $\theta_0 = 95°$. It was determined experimentally that $s_0 = 5$ provided the best fit to the data in this twilight region throughout the lunar cycle. The values of θ_0 and s_0 do not change between S_{max} and S_{min}.

The second scaling parameter, L_2, controls the lower asymptote of the EDS function, which represents night-time radiance values. Here, L_2 is allowed to vary as a function of lunar phase and lunar zenith angle and is defined differently between S_{max} and S_{min}. The minimum detectable signal of the DNB is near 2×10^{-10} W cm^{-2} sr^{-1}, so $L_{2_{\text{min}}}$ is chosen to yield values of $S_{\text{min}} \approx -10$ for night-time scenes. It is assumed that poorly reflective and dark backgrounds (e.g. shadows) will have similarly low radiance values regardless of the amount of moonlight. However, to improve contrast throughout the lunar cycle, $L_{2_{\text{min}}}$ is allowed to vary slightly as a function of the lunar zenith angle. For a lunar zenith angle, θ_{LZA}, given in degrees

$$L_{2_{\text{min}}} = 2.95 + 0.0022\theta_{\text{LZA}}. \tag{6}$$

Using this definition in Equation (5) yields values of R_{min} between 2×10^{-11} W cm^{-2} sr^{-1} at night during a new moon and 1.26×10^{-10} W cm^{-2} sr^{-1} at night during a full moon. Maximum radiance values at night are more highly variable. The brightest pixels are typically associated with city lights and fires, which can be several orders of magnitude brighter than the background during a new moon and this dominates the resulting images if R_{max} is set to these radiance values. Elsewhere, the observed radiance values may approach ~10^{-7} W cm^{-2} sr^{-1} during a full moon (Seaman et al., forthcoming) down to ~10^{-9} W cm^{-2} sr^{-1} due to airglow when moonlight is not present (Ingham 1971). To highlight clouds, snow, and other background surface features of importance to most operational users, city lights and fires are allowed to saturate (i.e. be assigned a brightness index value of 255). To account for additional variability in R_{max} between full moon and new moon, $L_{2_{\text{max}}}$ is defined as a function of both θ_{LZA} and the fraction of the lunar disc illuminated by the Sun, F_{LD}, as follows:

$$L_{2_{\text{max}}} = 2.65 + 0.0022\theta_{\text{LZA}} + 0.7(1 - F_{\text{LD}}), \tag{7}$$

where θ_{LZA} is, once again, given in degrees and F_{LD} is expressed as a decimal. F_{LD} is reported as a percentage in the geolocation files. Note that, given the definitions of $L_{2_{\text{max}}}$, S_{max}, and R_{max}, and accounting for the minus signs, the lunar illumination fraction yields the maximum night-time values of R_{max} during a full moon (where $F_{\text{LD}} \approx 1$), and the smallest night-time values of R_{max} during a new moon (where $F_{\text{LD}} \approx 0$) as desired.

The values of R_{max} and R_{min} based on the above definitions for the full-moon orbits are shown as the thick curves in Figure 2. Figures 4–6 show the radiance values as well as R_{max} and R_{min} as the functions of solar zenith angle for the last quarter, new moon, and first quarter orbits, respectively, using these definitions.

As a final step to ensure suitable image brightness across a wide variety of display platforms, a square-root correction is applied to the scaling function (Equation (2)) so that

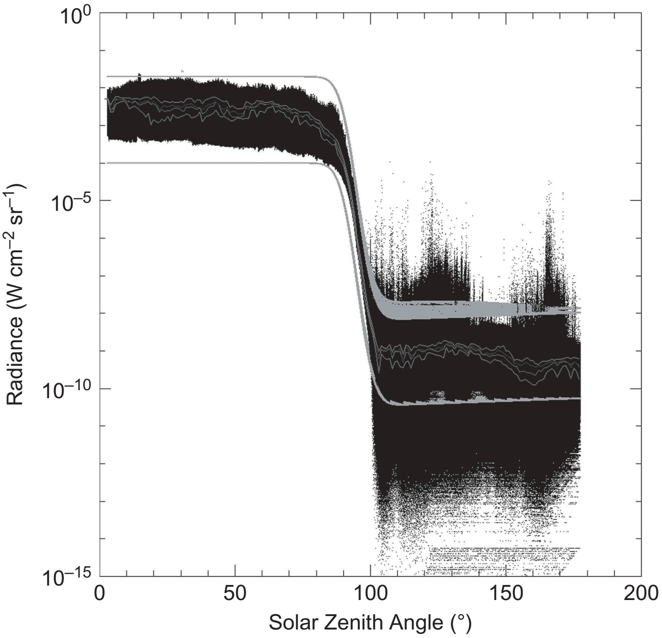

Figure 4. Same as in Figure 2, except for the last quarter orbits in Table 1.

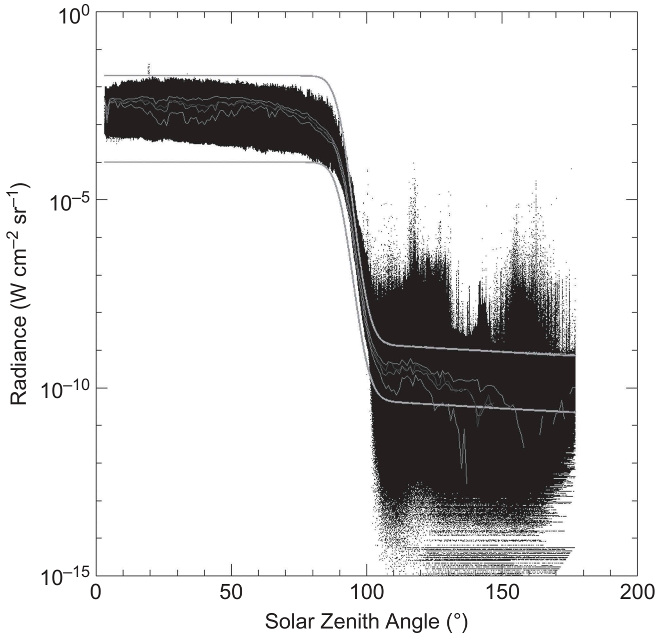

Figure 5. Same as in Figure 2, except for the new moon orbits in Table 1.

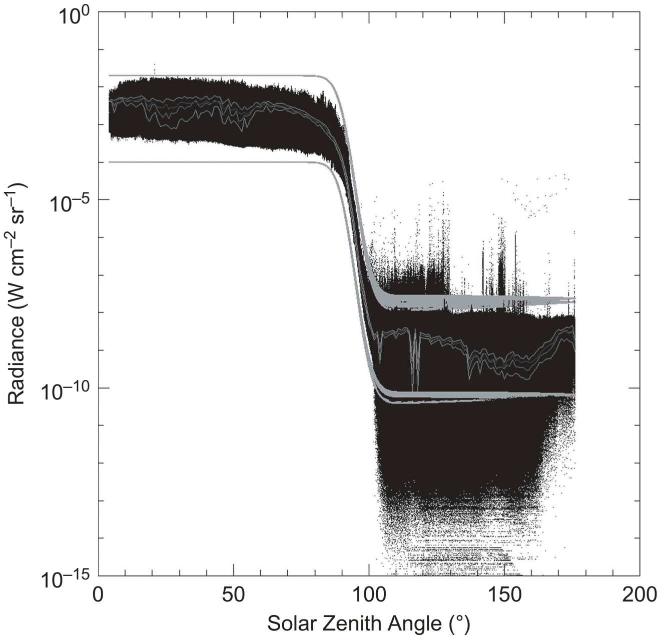

Figure 6. Same as in Figure 2, except for the first quarter orbits in Table 1.

$$B = 0 \leq 255 \times \sqrt{\left(\frac{R - R_{\text{min}}}{R_{\text{max}} - R_{\text{min}}}\right)} \leq 255. \tag{8}$$

This has the effect of augmenting the lowest brightness index values relative to the highest brightness index values and, in general, brightens the scene. This is similar to applying a 'gamma correction' with gamma equal to 2. Increasing the values of gamma above 2 would further brighten the darkest pixels, although this may lead to reduced contrast. Values of gamma less than 1 would darken the scene, with greater impact on the darkest pixels. It is possible that optimum brightness and contrast would require different values of gamma for specific display hardware.

4. Results

Although it is impractical to present imagery examples from all possible solar and lunar illumination conditions, here we present several examples of the EDS method that capture the expected range of illumination conditions from daytime to full moon to new moon and levels in-between. Caution must be exercised in the comparisons between the scaled DNB images and the NCC images shown, as the scaling method used to display the NCC product influences the perceived quality and usefulness of the images. The pseudo-albedo values in the NCC product are allowed to vary between −10 and 1000 to account for negative radiance values that may result from the dark-sky offsets in the DNB calibration (Geis et al. 2012) as well as radiance values that are up to three orders of magnitude larger than expected given the assumptions in the GVVSSE/GVVSLE tables (Liang et al. 2014). Using the maximum and minimum allowed values as the bounds for scaling NCC imagery results in very poor image contrast for the majority of scenes. Based on an analysis of NCC imagery for this study, pseudo-albedo values typically vary between 0 and 2 for daytime and night-time scenes. Pseudo-albedo values greater than 100 are possible in areas of city lights or fires at night during a new moon and, as with the DNB radiance values discussed in the previous section, these values can dominate the resulting images if the scaling bounds are not chosen properly. In the NCC images that follow, the pseudo-albedo values in the data files are scaled linearly between 0 (black) and 2 (white). The purpose of including NCC images here is to show how the EDS algorithm compares with the 'out-of-the-box' NCC product with no additional modifications by the user. Developing a method for the optimal display of NCC imagery is outside the scope of this work.

Figure 7 shows examples of the DNB imagery produced using the EDS method during both daytime and night-time for the full-moon case of 12 July 2014. Figure 7(*a*) was produced from the daytime overpass over northeast Africa, covering the area from southern Sudan to the eastern Mediterranean Sea. Figure 7(*b*) was produced from the night-time overpass and covers the area from extreme southern Libya to northwestern Angola. Except for the presence of city lights, the light from offshore oil activities, and lightning visible from a thunderstorm on the border between Niger and Nigeria,[2] it is difficult to distinguish at first glance which image in Figure 7 comes from daylight and which comes from moonlight. As the daytime portion of the EDS function (i.e. $\theta_{\mathrm{SZA}} < 85°$) does not change with the lunar cycle, Figure 7(*a*) is representative of the performance of the algorithm during typical (i.e. non-solar eclipse) daylight conditions.

An example of the EDS for a scene spanning the day/night terminator is shown along with the associated NCC image in Figure 8. These images are of Alaska from 13:23 UTC

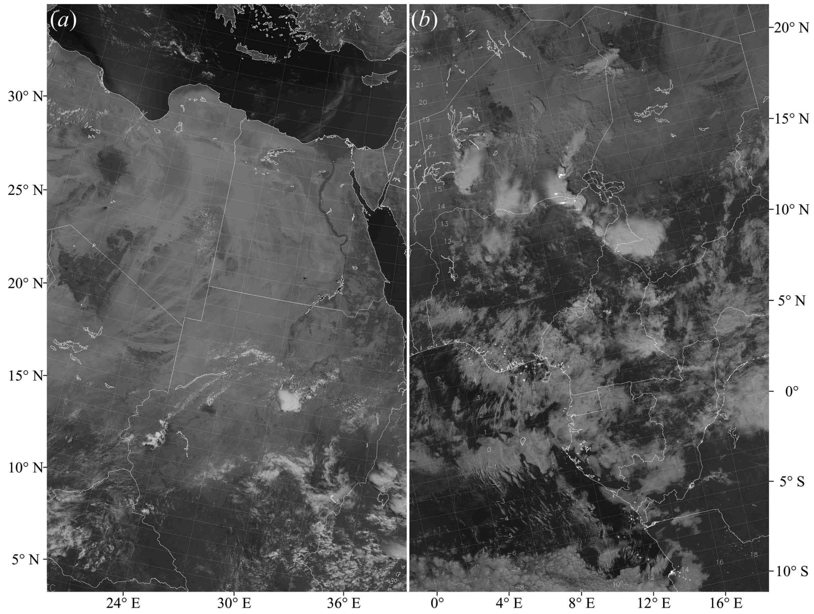

Figure 7. VIIRS DNB images produced using the EDS method for (*a*) daytime and (*b*) full moon at night lighting conditions. The image in (*a*) was produced from data collected near 11:43 UTC 12 July 2014. The image in (*b*) was produced from data collected near 00:35 UTC 12 July 2014.

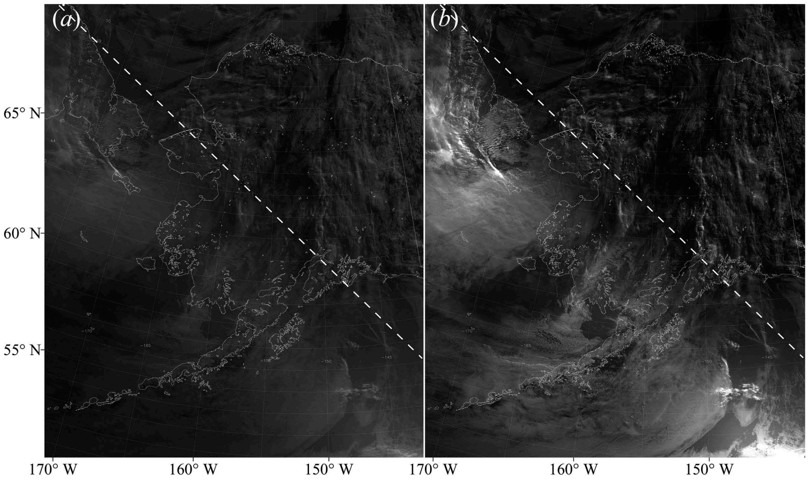

Figure 8. VIIRS DNB and NCC images of a twilight scene on the night following a last quarter moon (13:23 UTC 19 July 2014). (*a*) DNB image produced using the EDS method. (*b*) NCC image. The dashed lines in (*a*) and (*b*) represent the 89° solar zenith angle contour with daylight in the upper right corner and night in the lower left corner.

19 July 2014, a date and time that are outside the test data set described in Table 1. The 89° solar zenith angle contour is plotted as the dashed lines in Figure 8. This line represents the limit at which other VIIRS visible and near-IR channels record data as the satellite approaches the day/night terminator. Pixels north and east of the dashed line are directly illuminated by the Sun, whereas points south and west of the line transition from twilight to night-time. In this case, the data for these images were collected the night following a last quarter moon. In both images of Figure 8, side-illumination of clouds and atmospheric scattering contribute to elevated brightness values in the twilight region, although these effects are exaggerated in the NCC image (Figure 8(*b*)). Nevertheless, both NCC and EDS algorithms reveal clouds and other features with relatively similar contrast on both day and night sides of the terminator.

Figure 9 shows an example of a DNB image produced using the EDS method along with base-10 logarithmic scaling (similar to Figure 1(*b*)) and the associated NCC image for the case of a new moon at night over the Pacific Ocean. These images cover the latitude range from 36° N to 2° S and the longitude range from 153° W to 177° E. The Hawaiian Islands are visible in the upper right quadrant of the images at the edge of the swath. During a new moon, no moonlight is available to illuminate clouds and other features. In Figure 9(*a*), the clouds are visible due to illumination by airglow (see, e.g., Miller, Mills, et al. 2012). These clouds are not visible in the logarithmic scaling (Figure 9 (*b*)) as the city lights from the Hawaiian Islands are three to four orders of magnitude brighter than airglow, and these city lights dominate the scaling. Clouds are also difficult to see in the associated NCC image (Figure 9(*c*)) as the pseudo-albedo values are very low – generally less than 0.25 outside the city lights – suggesting the NCC algorithm has difficulty accounting for airglow. Clouds illuminated by sunlight and moonlight typically have pseudo-albedo values closer to 1 in the NCC imagery in other cases that were examined in this work. It should be noted that airglow is an illumination source that was not considered in the design of the NCC algorithm, as it was not known prior to launch that the DNB had the sensitivity to detect it (Liang et al. 2014). Whereas the scaling used

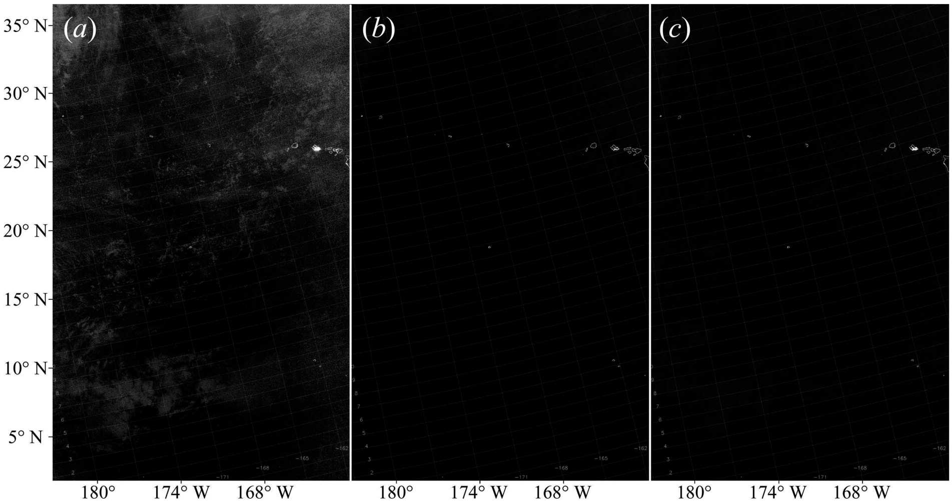

Figure 9. VIIRS DNB and NCC images taken at night during a new moon (13:01 UTC 26 July 2014). (*a*) DNB image produced using the EDS method. (*b*) DNB image produced using simple logarithmic scaling. (*c*) NCC image. In each panel, the Hawaiian Islands are visible on the right edge above the centre.

to display the NCC image may be improved to reveal the cloud structures in this case, it is apparent that the EDS is suitable for revealing clouds illuminated only by airglow – extending the utility of night-time low-light visible imagery to the ~50% of night-time passes without moonlight.

Figure 10 shows a sequence of night-time DNB images produced using the EDS method at varying phases of the lunar cycle. The associated NCC images are shown in Figure 11. Data for these images were collected from night-time overpasses during October and November 2014. The images show the coast of California, which is a region of persistent marine stratocumulus clouds. Although the marine stratocumulus clouds have been pushed offshore in Figures 10(*b*) and (*c*) and 11(*b*) and (*c*), both EDS DNB and NCC images have sufficient contrast to detect these clouds and this contrast is maintained throughout the lunar cycle. Note that no moonlight is present in Figures 10(*a*) and (*b*) and 11(*a*) and (*b*) as these images were taken between a new moon and a first quarter moon.

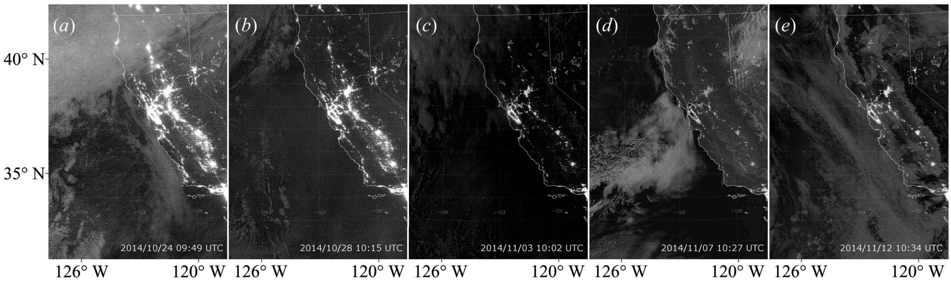

Figure 10. VIIRS DNB images utilizing the EDS method showing the coast of California at night at varying phases during a lunar cycle: (*a*) waxing 2% full; (*b*) waxing 30% full; (*c*) waxing 91% full; (*d*) waning 98% full; and (*e*) waning 63% full.

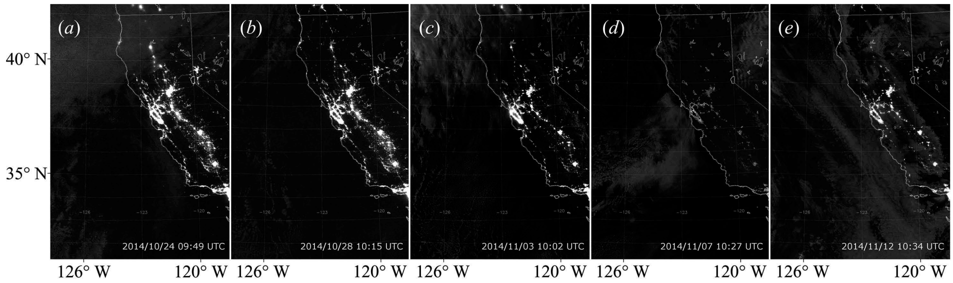

Figure 11. Same as in Figure 10, except for the NCC images that are shown.

5. Conclusions

In this work, a new dynamic scaling algorithm, referred to as the ‘erf-dynamic scaling (EDS) algorithm’, was developed for the purpose of displaying VIIRS DNB SDR data as images under all natural lighting conditions (day, night, and twilight) throughout the lunar cycle. The EDS algorithm uses the Gauss error function to relate maximum and minimum expected radiance values to the solar and lunar zenith angles and the fraction of the lunar disc that is illuminated by the Sun. This algorithm requires only information available to users in the SDR data and geolocation files that are produced and distributed according to the JPSS file standards. No ancillary information is required.

Using this algorithm under full-moon conditions, imagery produced at night has a similar appearance to imagery produced during the day. This algorithm also provides sufficient contrast to detect clouds illuminated only by airglow, which occurs anytime the moon is well below the horizon during the night-time overpass (this accounts for half of the lunar cycle). In twilight scenes or scenes spanning the day/night terminator, the EDS algorithm achieves an image quality similar to or, in some cases, exceeding the operational NCC EDR imagery product. This work has shown that it is possible to approximate the NCC algorithm directly from the DNB SDR data files without using GVVSSE/GVVSLE tables or other ancillary information.

This dynamic scaling algorithm is expected to benefit operational users that, for practical reasons under the current configuration, are unable to acquire the operational NCC EDR product. This algorithm is also expected to benefit users that would otherwise rely on *ad hoc* methods for displaying DNB data as this single algorithm produces nearly constant contrast from day to night with no modification throughout the lunar cycle. Furthermore, there are currently no plans within the JPSS program to reprocess NCC data prior to the implementation of the current version of the NCC algorithm, which occurred on 10 July 2013. The EDS algorithm may be used to provide NCC-like imagery directly from the DNB SDRs for cases prior to this date, although stray-light artefacts would be apparent for such scenes near the terminator. The DNB stray-light correction was implemented operationally concurrent with the improvements to the NCC algorithm.

High latitude locations (poleward of ~60° latitude) are typically outside the view of geostationary satellites and users in these areas rely upon the relatively high frequency of polar-orbiting satellite overpasses to provide timely observations of the atmosphere and background surface. In these locations, the day/night terminator is an ever-present feature during the ‘daytime’ overpasses near the winter solstice and the ‘night-time’ overpasses near the summer solstice. The ability to view DNB imagery with nearly constant contrast across the day/night terminator is a benefit to these users.

Similar to the NCC EDR algorithm (Liang et al. 2014), there are several limitations of the EDS algorithm. The presence of side-illumination of clouds and snow/ice-covered terrain in the twilight region and the presence of the aurora at night where there is little to no moonlight may result in radiance values several orders of magnitude greater than can be predicted when assuming the radiance values are only a function of solar and lunar zenith angles. In addition, atmospheric scattering also leads to anomalous brightening in the twilight region that both EDS and NCC algorithms do not account for. Although it may be possible to improve these algorithms by accounting for atmospheric scattering in the twilight region, side-illumination of highly reflective surfaces and the aurora are highly variable from one orbit to another and any correction to account for this would likely be scene-dependent. For localized scenes, it may be possible to adjust R_{max} up or down based on the percentage of pixels within the scene that are at or near saturation.

It was also discovered during the course of this work that the fraction of the lunar disc illuminated by the Sun (F_{LD}) that is reported in the DNB geolocation files does not account for lunar eclipses. During the total lunar eclipse of 8 October 2014, values of F_{LD} were above 99%, even at the peak of the eclipse. This will negatively impact the quality of the resulting DNB images produced during a lunar eclipse. The EDS algorithm also does not account for solar eclipses.

These concerns, however, are limited to relatively small areas of the globe, or to relatively short time periods and are similar between the scaling algorithm developed here and the already-operational NCC algorithm.

Acknowledgements

The authors would like to acknowledge the contributions of Dan Lindsey and Don Hillger (NOAA/Satellite Applications and Research) and other members of the VIIRS Imagery and Visualization Team for providing valuable feedback, suggestions, and constructive criticism. The thoughtful comments and suggestions provided by the anonymous reviewers are also acknowledged.

Disclosure statement

No potential conflict of interest was reported by the authors.

Funding

This work was supported by the National Oceanic and Atmospheric Administration [grant number NA14OAR4320125 Amd#17].

Notes

1. NCEP (National Center for Environmental Prediction) Advanced Weather Interactive Processing System (Schotz et al. 2008).
2. Lightning appears as linear streaks in the data due to the scanning nature of the DNB instrument. See, e.g. Miller et al. (2013).

References

Geis, J., C. Florio, D. Moyer, K. Rausch, F. De Luccia, J. J. Butler, X. Xiong, and X. Gu. 2012. “VIIRS Day-Night Band Gain and Offset Determination and Performance.” *Proceedings SPIE Earth Observing Systems XVII* 8510: 851012. doi:10.1117/12.930078.

Hillger, D., T. Kopp, T. Lee, D. Lindsey, C. Seaman, S. Miller, J. Solbrig, S. Kidder, S. Bachmeier, T. Jasmin, and T. Rink. 2013. "First-Light Imagery from Suomi NPP VIIRS." *Bulletin American Meteorology Society* 94: 1019–1029. doi:10.1175/BAMS-D-12-00097.1.

Ingham, M. F. 1971. "The Light of the Night Sky and the Interplanetary Medium." *Reports on Progress in Physics* 34 (3): 875–912. doi:10.1088/0034-4885/34/3/302.

Lee, T. E., S. D. Miller, J. Turk, C. Schueler, R. Julian, S. Deyo, P. Dills, and S. Wang. 2006. "The NPOESS VIIRS Day/Night Visible Sensor." *Bulletin American Meteorology Social* 87: 191–199. doi:10.1175/BAMS-87-2-191.

Liang, C. K., S. Mills, B. I. Hauss, and S. D. Miller. 2014. "Improved VIIRS Day/Night Band Imagery with Near Constant Contrast." *IEEE Transactions on Geoscience and Remote Sensing* 52 (11): 6964–6971. doi:10.1109/TGRS.2014.2306132.

Liao, L. B., S. Weiss, S. Mills, and B. Hauss. 2013. "Suomi NPP VIIRS Day-Night Band On-Orbit Performance." *Journal of Geophysical Research: Atmospheres* 118: 12,705–12,718. doi:10.1002/2013JD020475.

Miller, S. D., C. L. Combs, S. Q. Kidder, and T. F. Lee. 2012. "Assessing Global and Seasonal Lunar Availability for Night-Time Low-Light Visible Remote Sensing Applications." *Journal of Atmospheric and Oceanic Technology* 29 (4): 538–557.

Miller, S. D., S. P. Mills, C. D. Elvidge, D. T. Lindsey, T. F. Lee, and J. D. Hawkins. 2012. "Suomi Satellite Brings to Light a Unique Frontier of Nighttime Environmental Sensing Capabilities." *Proceedings of the National Academy of Sciences* 109 (39): 15706–15711. doi:10.1073/pnas.1207034109.

Miller, S. D., W. Straka III, S. P. Mills, C. D. Elvidge, T. F. Lee, J. Solbrig, A. Walther, A. K. Heidinger, and S. C. Weiss. 2013. "Illuminating the Capabilities of the Suomi National Polar-Orbiting Partnership (NPP) Visible Infrared Imaging Radiometer Suite (VIIRS) Day/Night Band." *Remote Sensing* 5: 6717–6766. doi:10.3390/rs5126717.

Miller, S. D., and R. E. Turner. 2009. "A Dynamic Lunar Spectral Irradiance Dataset for NPOESS/VIIRS Day/Night Band Night-Time Environmental Applications." *IEEE Transactions on Geoscience and Remote Sensing* 47 (7): 2316–2329. doi:10.1109/TGRS.2009.2012696.

Mills, S. P., S. C. Weiss, and C. K. Liang. 2013. "VIIRS Day/Night Band (DNB) Stray Light Characterization and Correction." *SPIE Optical Engineering Applications* 8866: 88661P-1–88661P-18.

Mills, S. P., S. C. Weiss, T. Ohnuki, D. Searcy, M. Plonski, E. Jacobson, J. McCarthy, and J. Jaron, 2010. "Calibration of the VIIRS Day/Night Band (DNB)." Proceedings of AMS 6th Annual Symposium Future National Operational Environmental Satellite Systems-NPOESS-GOES-R, 1–9, American Meteorology Society, Atlanta, GA.

Schotz, S., J. P. Tuell, S. Jacobs, D. Plummer, S. Gilbert, and R. Henry, 2008. "Integrating NAWIPS into the New NWS Service Oriented Architecture," Proceedings of AMS 24th Conference IIPS, American Meteorology Society, New Orleans, LA.

Seaman, C., D. Hillger, T. Kopp, R. Williams, S. Miller, and D. Lindsey. Forthcoming. "Visible Infrared Imaging Radiometer Suite (VIIRS) Imagery Environmental Data Record (EDR) User's Guide." In *NOAA Technical Report*. Washington, DC: National Oceanic and Atmospheric Administration.

Seguin, W. R., 2002. "AWIPS. an End-To-End Look" Proceedings of AMS 18th International Conference IIPS, American Meteorology Society, Orlando, FL, J47–J51.